

Strategies to search for two-dimensional materials with long spin qubit coherence time

Michael Y. Toriyama^{a*}, Jiawei Zhan^b, Shun Kanai^{c,d,e,f}, and Giulia Galli^{a,b*}

Two-dimensional (2D) materials that can host qubits with long spin coherence time (T_2) have the distinct advantage of integrating easily with existing microelectronic and photonic platforms, making them attractive for designing novel quantum devices with enhanced performance. However, the relative lack of 2D materials as spin qubit hosts, as well as appropriate substrates that can help maintain long T_2 , necessitates a strategy to search for candidates with robust spin coherence. Here, we develop a high-throughput computational workflow to predict the nuclear spin bath-driven qubit decoherence and T_2 in 2D materials and heterostructures. We initially screen 1173 2D materials and find 190 monolayers with $T_2 > 1$ ms, higher than that of naturally-abundant diamond. We then construct 1554 lattice-commensurate heterostructures between high- T_2 2D materials and select 3D substrates, and we find that T_2 is generally lower in a heterostructure than in the bare 2D host material; however, low-noise substrates (such as CeO_2 and CaO) can help maintain high T_2 . To further accelerate the material screening effort, we derive analytical models that enable rapid predictions of T_2 for 2D materials and heterostructures. The models offer a simple, yet quantitative, way to determine the relative contributions to decoherence from the nuclear spin baths of the 2D host and substrate in a heterostructural system. By developing a high-throughput workflow and analytical models, we expand the genome of 2D materials and their spin coherence times for the development of spin qubit platforms.

1 Introduction

Spin defects in solid-state materials offer a promising platform for realizing qubit-based technologies. However, the loss of phase information between the defect's levels due to the environment can significantly reduce the reliability of a qubit and, as a result, limit the performance of a quantum device. In the regime where the dephasing rate significantly exceeds the relaxation rate, the qubit's decoherence is characterized by the time it takes to lose memory of its phase (called decoherence time T_2). Decoherence can occur due to a number of reasons. In solids, magnetic noise from nuclear isotopes can play a major role. As a result, the choice of the host material, which determines the nuclear spin environment of the qubit, is an important design consideration that strongly affects the performance of quantum devices.

Many three-dimensional (3D) materials have been studied as spin qubit hosts, including diamond, silicon carbide, and oxides, which are systems with relatively low magnetic noise. However, in many applications, in particular quantum sensing, the spin defect needs to be placed near the surface of the material, where dangling bonds and surface defects can introduce additional un-

wanted noise leading to decoherence.¹ Two-dimensional (2D) materials, on the other hand, offer distinct advantages over 3D qubit hosts, for example the density of nuclear isotopes is inherently lower than in 3D materials, thus limiting the decoherence from magnetic noise.^{2,3} In addition, if 2D monolayers can be exfoliated from 3D van der Waals-bonded layered systems, the decoherence due to dangling bonds can be greatly limited. Atomically-precise creation of spin defects on monolayers has been demonstrated using, e.g., scanning tunneling microscopy,⁴⁻⁶ enabling precise control over functional properties. Further, 2D materials can be integrated with microelectronic and photonic platforms,⁷ possibly enabling the design of devices with enhanced capabilities and/or novel functionalities.

Studies of qubits in 2D materials have so far been limited to few platforms, such as h-BN, transition metal dichalcogenides, and recently GeS_2 .⁸⁻¹¹ In order to realize quantum devices equipped with specific functions, a substantially wider selection of 2D host materials is desirable. In a previous report, the Hahn echo T_2 times of 69 spin defects in 45 2D host materials were calculated,¹² offering important insights into the spin coherence properties of 2D materials. However, to gain a deeper understanding of these properties, and include the effect of the substrate over which 2D materials reside, a much broader set of systems need to be considered. Critically, the existing literature lacks data-driven insights into substrate-induced decoherence effects in heterostructural qubit hosts. In addition, while a model of T_2 was recently developed to rapidly screen thousands of potential 3D qubit host materials,¹³ no such model is available for 2D systems. Such a model can accelerate predictions of T_2 for large sets of materials, and even possibly enable AI-assisted design of materials with robust spin qubit coherence.

^aMaterials Science Division, Argonne National Laboratory, Lemont, IL 60439, USA.

^bPritzker School of Molecular Engineering, University of Chicago, Chicago, IL 60637, USA.

^cLaboratory for Nanoelectronics and Spintronics, Research Institute of Electrical Communication, Tohoku University, Sendai 980-8577, Japan.

^dWPI-Advanced Institute for Materials Research (WPI-AIMR), Tohoku University, Sendai 980-8577, Japan.

^eNational Institutes for Quantum Science and Technology, Takasaki 370-1207, Japan.

^fDivision for the Establishment of Frontier Sciences, Tohoku University, Sendai 980-8577, Japan.

*E-mail: mtoriyama@anl.gov, gagalli@uchicago.edu

Here, we develop and implement a computational strategy to search for 2D materials and heterostructural systems with appropriate substrates which can maintain long coherence times. We compute the spin-echo T_2 time using the cluster correlation expansion (CCE) approach.¹⁴ A key capability developed in our work is an automated framework to perform CCE simulations with little manual intervention, enabling large-scale predictions of T_2 for a vast set of materials. We initially apply this approach to 1173 2D materials sourced from the MC2D database, finding 190 monolayers with $T_2 > 1$ ms. We find that 2D materials with the 15 highest predicted T_2 all have a band gap greater than 2 eV, suggesting that they can host defect-induced electronic levels within their band gap to realize a spin qubit. We then construct 1554 heterostructures between high- T_2 monolayers and 3D substrates with commensurate lattices. Our data-driven approach correctly predicts that qubit coherence can be limited by either the 2D host material or the substrate, depending on the material with the noisier nuclear spin environment. Using our data, we propose physically-motivated models of T_2 for 2D materials and heterostructures, enabling rapid predictions of coherence times from only structural information. We apply the model to 2D materials sourced from several databases, allowing us to expand our search space by 4740 additional monolayers.

Prior to describing our results, we make a few important remarks on nomenclature. First, we note that monolayers considered in this work are not all strictly two-dimensional and are instead few atoms thick. However, we will refer to them as “2D materials” and “monolayers” interchangeably to reflect their small thickness, which is a key property than enables long coherence times due to the low nuclear spin density.² Second, when it is stated that a material “exhibits high/long T_2 ”, this refers to the fact that the material can *accommodate a spin qubit with long T_2* . While T_2 is, strictly speaking, a property of the spin defect/qubit, we attribute it to the host material in this study to reflect the decoherence effects through hyperfine interactions with the nuclear spin bath.

2 Results

2.1 High-throughput workflow

We show in Figure 1a our tiered computational workflow for identifying 2D host materials and heterostructures with long Hahn-echo coherence time (T_2). Broadly, the workflow is composed of two stages: we first identify 2D materials with high T_2 , which are then combined with 3D substrates and screened for high- T_2 heterostructures. This is motivated by the idea that high T_2 for the monolayer is essential, because the substrate will introduce additional noise to the qubit and lead to lower T_2 in a heterostructural system. We show in Section 2.3 that this hypothesis is largely valid, where calculations show that T_2 of heterostructures are generally lower than that of the base 2D host material.

Description of 2D materials set. With the rise of material informatics, several 2D materials databases have been developed in recent years.^{15–20} For the purposes of experimental realization, it is important to consider realistic 2D materials. While various thermodynamic arguments can be made to demonstrate the stability

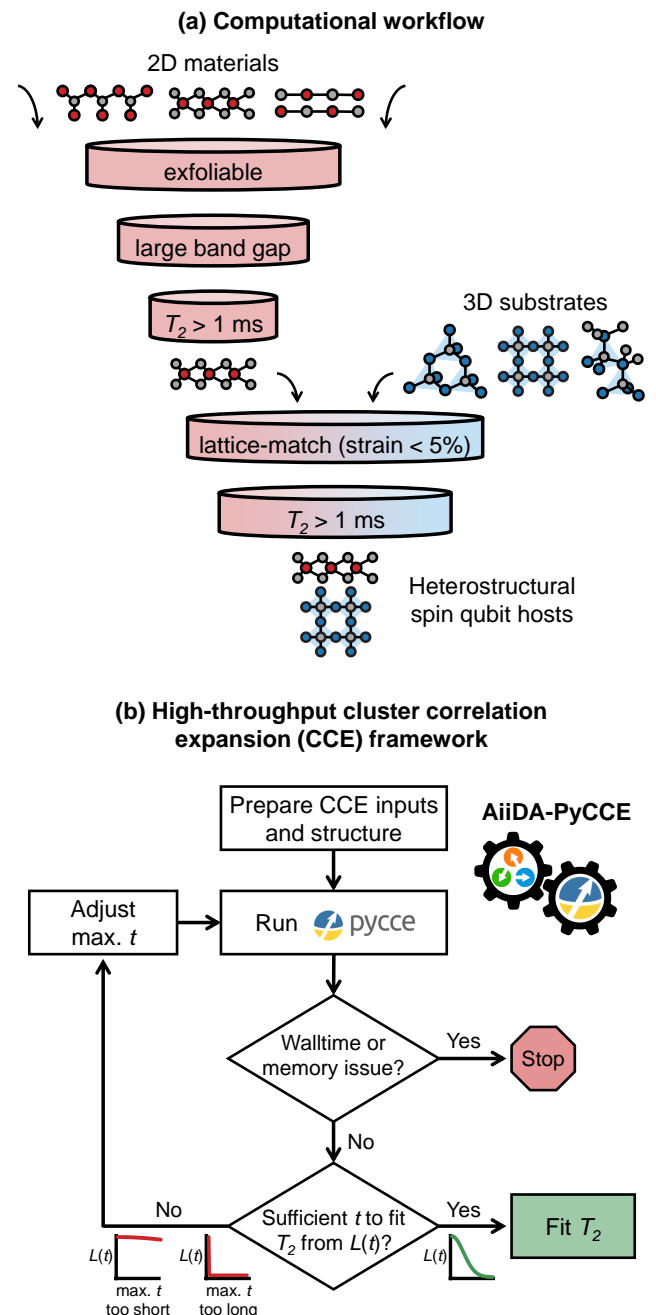


Figure 1. Computational methodology. (a) The workflow for screening 2D materials and heterostructures with long coherence times (T_2) adopted in this work. Promising 2D materials with high T_2 times are identified initially, followed by the creation and screening of heterostructures. (b) The automated methodology for performing cluster correlation expansion (CCE) simulations to calculate T_2 devised in this work.

of a hypothetical 2D material, perhaps a more effective strategy is to consider monolayers that can be exfoliated from *known* materials.

Therefore, in our work, we consider 2D materials that are curated by the MC2D database.^{15,16,21} This database offers the distinct advantage of compiling monolayers that are isolated from 3D layered materials that are *experimentally-known*, and are

sourced from experimental crystal structure databases such as ICSD,^{22,23} COD,^{24,25} and MPDS.²⁶ Key properties that indicate whether a monolayer can be exfoliated from its corresponding 3D parent phase, such as the binding energy, are calculated and recorded in the database. Although many of the monolayers are still hypothetical, in that they have not yet been experimentally realized in monolayer form, comparing binding energies to those of monolayers that have been successfully realized (e.g., h-BN and graphene) enables us to identify those that can potentially be exfoliated in experiments. In particular, we consider materials that have DFT binding energy that is less than 130 meV/Å² when calculated using the DF2-C09 and rVV10 functionals, which are considered either “easily” or “potentially” exfoliable in Ref. 15.

Additionally, realizing spin qubits materials with wide band gaps is ideal, because these materials can potentially accommodate localized defect states in the band gap which do not interfere with host states.²⁸ The band gap of each monolayer in the MC2D database is predicted using the generalized gradient approximation (GGA), which typically underestimates the measured band gap of a material. To ensure that we consider systems with sufficiently wide band gaps without missing potential spin qubit hosts, we consider materials with a GGA band gap greater than 0.5 eV in our work. We then refine our band gap predictions of monolayers with the highest T_2 times by using the screened-exchange range-separated hybrid (SE-RSH) functional, which yield higher accuracy results for solids and interfaces^{29,30}

Automated framework for performing cluster correlation expansion simulations. A key capability gap addressed in this work is a high-throughput framework to calculate the T_2 coherence times of a large set of materials. We use the cluster correlation expansion (CCE) approach, as implemented in the open-source PyCCE code,³¹ to simulate the decoherence dynamics of a spin qubit in the presence of nuclear isotopes in a host material. The CCE method allows us to calculate the coherence function $\mathcal{L}(t)$ of a spin qubit, from which the T_2 time can be extracted by fitting $\mathcal{L}(t)$ to a stretched exponential form, $\mathcal{L}(t) = \exp[-(t/T_2)^n]$. More details can be found in Section 4.

For each CCE calculation, the maximum time and number of time steps to simulate $\mathcal{L}(t)$ must be decided. Ideally, the number of time steps will be sufficiently large to obtain enough information on $\mathcal{L}(t)$, but an arbitrarily large number of steps would lead to walltime and/or memory issues. Moreover, the maximum simulation time cannot be too short nor arbitrarily long, otherwise the simulated $\mathcal{L}(t)$ will be incomplete or would decay too early within the simulated time domain, respectively (Figure 1b). In either case, one cannot obtain a reliable fit of T_2 . As a result, a workflow manager that can track each simulation is needed, especially when handling a large set of materials.

Here, we built a software based on the AiiDA workflow manager^{32,33} to run PyCCE in a high-throughput manner (Figure 1b). The software, which we call AiiDA-PyCCE,³⁴ initializes each calculation from only the structure of a material and basic CCE inputs. A key feature of this software is the ability to automatically check each simulation to ensure it ran for an appropriate time (Figure 1b), thus enabling reliable fits of T_2 with no manual in-

tervention. Using our high-throughput framework, we identify materials with $T_2 > 1$ ms (Figure 1). We choose this bound to be similar to that of naturally-abundant diamond, which has a coherence time of $T_2 \sim 0.9$ ms when calculated using similar CCE methods.¹³

Once 2D materials with long T_2 time have been identified, heterostructures are created between them and 3D substrates cleaved along different planes (Figure 1a). The list of substrates considered in this study is given in Table S1. We create heterostructures where the interlayer separation between the 2D host and substrate is set to the sum of van der Waals radii³⁵ of the atoms at the interface. We also ensure that the lattices are commensurate by applying a strain no greater than 5% to the 2D material, using an algorithm proposed by Zur and McGill³⁶ and implemented in the MPInterfaces code.³⁷ The lattice commensurability requirements depend on the type of bonding at the heterointerface. If the 2D material is chemically bonded (e.g. covalently) to the substrate, then the lattice will likely become strained to accommodate the interfacial bonds, thus enforcing lattice commensurability. On the other hand, if the 2D material is weakly bound to the substrate through van der Waals forces, we can expect the lateral strain on the monolayer to be minimal, even when the lattices themselves are incommensurate.³⁸ However, lattice incommensurability leads to technical problems for *ab initio* methods with periodic boundary conditions, where a repeatable unit cell must be defined. Lattice-matching ensures that each heterointerface can be defined within a cell of finite size, thus enabling *ab initio* calculations of these heterostructures. We do not relax the interfacial structure to ensure that the workflow can be executed in a high-throughput manner. We show in Section 2.3 and the Supplemental Information that this is largely justified by the relative insensitivity of the nuclear spin bath-induced decoherence to specific details of the interfaces considered in our study, such as the interlayer separation, strain, and atomic reconstruction.

2.2 Coherence time T_2 of 2D materials

Out of 1173 monolayers, we find 190 monolayers that exhibit $T_2 > 1$ ms using our high-throughput workflow. The top 15 candidates are shown in Table 1, along with their band gaps calculated using the screened-exchange range-separated hybrid (SE-RSH) functional,^{29,30} the ID in the MC2D database, and the experimental details of the 3D parent phase from which the monolayer can be exfoliated. Although we only consider monolayers with GGA band gap greater than 0.5 eV in our screening (see Section 2.1), our calculations with the SE-RSH functional show that monolayers with the 15 highest T_2 have band gaps greater than 2 eV (Table 1). It may therefore be possible to realize a spin qubit with a localized two-level system through doping in each of these monolayers. For reference, WS₂, which has been used as a spin qubit platform,⁴⁻⁶ has a predicted band gap of 2.61 eV in monolayer form (Table 1), in agreement with other quasiparticle calculations (2.9–3.1 eV)^{39,40} and experimental values (2.4–2.7 eV).^{41,42}

Our results generally support the conclusion that 2D materials

Table 1. 2D materials with the 15 highest spin coherence times (T_2) identified using our computational workflow. The monolayers are sourced from the Materials Cloud 2D crystals database (MC2D) with their IDs listed, the coherence time is calculated from cluster correlation expansion (CCE) simulations, and the band gap is predicted using the screened-exchange range-separated hybrid (SE-RSH) functional. For each 2D host material, there is a corresponding 3D layered phase that is experimentally known; we list the database and ID number for each parent phase.

2D host	T_2 (ms)	E_g (eV)	MC2D ID	Exp. database	Exp. ID	Notes
WS ₂	35.4	2.61	234	COD	9009145	Well-known ^{5,6}
Au ₂ Se ₃ O ₁₀	23.5	4.17	1214	COD	4311594	
Au ₂ Se ₂ O ₇	16.2	4.16	1205	COD	7209412	
PdSO ₄	14.8	3.81	2224	ICSD	79559	Successfully exfoliated ²⁷
Hg ₂ GeO ₄	14.2	5.6	1451	ICSD	26340	
AgCO ₂	14.0	5.32	377	ICSD	109600	
KNO ₃	11.7	8.23	1667	ICSD	384	
KAgTeS ₃	11.6	3.49	2040	MPDS	S1804089	
K ₂ Ag ₂ GeS ₄	11.2	4.32	922	ICSD	170843	
AuSe	10.6	2.07	14	COD	1510294	β -phase
PbSO ₃	10.5	5.75	656	COD	9009622	
K ₂ Ge ₂ S ₅	10.1	4.89	1850	ICSD	411027	
GeS ₂	9.9	3.19	1951	MPDS	S1831556	High-pressure tetragonal phase
PbSeO ₃	9.8	6.11	1279	COD	1526029	
GeS	9.6	2.78	159	COD	9008784	

can accommodate longer T_2 times than 3D materials. By comparing the T_2 times of 2D monolayers against their corresponding 3D parent phases, we find that 2D materials generally exhibit longer T_2 times (Figure 2a). This can be attributed to their low dimensionality and, as a result, inherently lower nuclear spin density.

The monolayer with the highest predicted T_2 is WS₂ ($T_2 = 35.4$ ms, Table 1), which has been tested as a spin qubit platform.⁴⁻⁶ The high T_2 can be attributed to the relatively low g -factor of ¹⁸³W (0.24) and the low nuclear spin density of ³³S (0.76%). In fact, we find that many high- T_2 materials are oxides or sulfides, with some even being heteroanionic with two or more chalcogen species (Table 1 and Figure S1), owing to the low natural abundance of isotopes with nonzero spin, specifically ¹⁷O (0.038%).

and ³³S (0.76%). A similar conclusion has been drawn for 3D solids.¹³

The Au-oxselenide monolayers Au₂Se₃O₁₀ ($T_2 = 23.5$ ms) and Au₂Se₂O₇ ($T_2 = 16.2$ ms) exhibit the second- and third-highest T_2 times in our list. Although ¹⁹⁷Au is a spinful nuclear species ($S = 3/2$) with 100% natural abundance, the relatively low nuclear g -factor (0.097) and large interatomic separation enables high T_2 in these host materials. The oxygen-rich chemical makeup is also beneficial for spin coherence due to the low natural abundance of the ¹⁷O isotope. Note that there are corner-sharing units of square-planar AuO₄ and units of SeO₃ in both structures (Figures 2c and 2d), as well as near-tetrahedral units of SeO₄ in Au₂Se₃O₁₀ (Figure 2c). As tabulated in the MC2D database, the

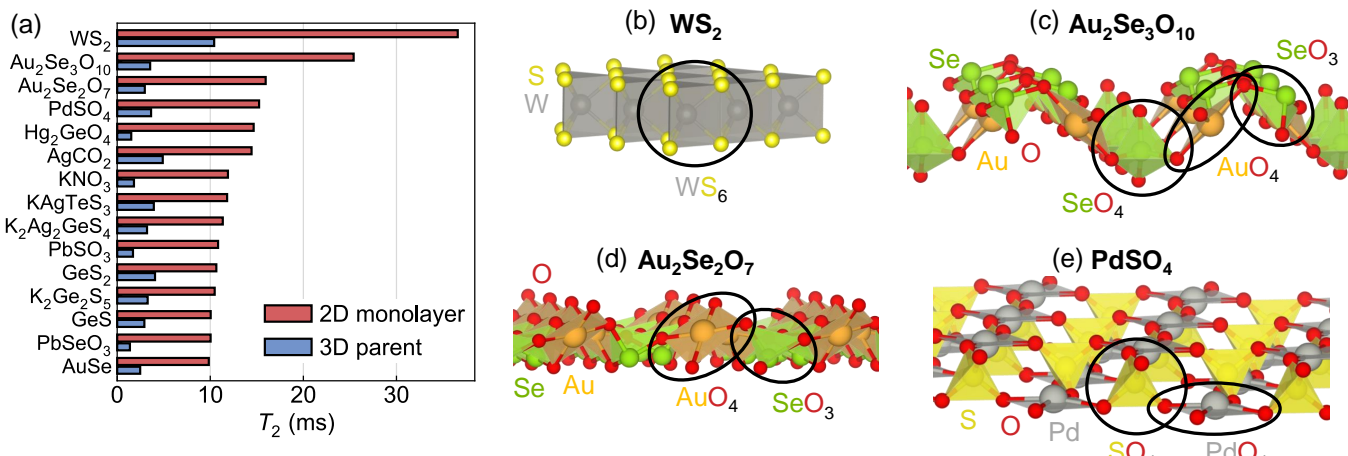


Figure 2. 2D materials with high coherence time. (a) Comparison of spin coherence time (T_2) for qubits implanted in 2D monolayers (red) and corresponding 3D parent phases (blue). 2D materials can generally accommodate spin qubits with longer coherence time than their 3D parent phase. Structures of monolayers with the highest T_2 are shown, namely (b) WS₂, (c) Au₂Se₃O₁₀, (d) Au₂Se₂O₇, and (e) PdSO₄.

binding energies of the two compounds ($E_b = 27.6 \text{ meV}/\text{\AA}^2$ for $\text{Au}_2\text{Se}_3\text{O}_{10}$ and $E_b = 27.3 \text{ meV}/\text{\AA}^2$ for $\text{Au}_2\text{Se}_2\text{O}_7$) are comparable to that of PtSe_2 ($E_b = 29.6 \text{ meV}/\text{\AA}^2$), which has been successfully exfoliated through mechanical^{43,44} and electrochemical⁴⁵ means. This suggests that both Au-oxyselelenide monolayers can also be exfoliated from their respective 3D layered parent phases.

We find that PdSO_4 is another candidate spin qubit host with high T_2 (14.8 ms), which can be attributed to the low nuclear spin densities of ^{17}O and ^{33}S , as well as the relatively low nuclear g -factor of ^{105}Pd (-0.257), an isotope that exists with 22.33% natural abundance. The structure is embedded with units of tetrahedral SO_4 and square-planar PdO_4 (Figure 2e).⁴⁶ Sheets of PdSO_4 with ~ 3 nm thickness were recently synthesized through liquid-phase exfoliation,²⁷ demonstrating potential for near-term testing as a spin qubit host. This is perhaps not surprising given the low binding energy of the material ($E_b = 8.54 \text{ meV}/\text{\AA}^2$), which is lower than that of graphene ($E_b = 20.29 \text{ meV}/\text{\AA}^2$) and MoS_2 ($E_b = 21.56 \text{ meV}/\text{\AA}^2$).^{15,16}

$\beta\text{-GeS}_2$ (space group $P2_1/c$) has recently been gaining traction as a potential spin qubit host at ambient conditions.^{10,11} Although monolayer $\beta\text{-GeS}_2$ is not listed in the MC2D database, we find that a monolayer of the high-pressure tetragonal phase of GeS_2 (space group $P4_2/nmc$) has $T_2 = 9.9$ ms (Table 1). Separately, we isolate a monolayer from the 3D layered phase of $\beta\text{-GeS}_2$ found in the Materials Project database (mp-572892) and find that it possesses $T_2 = 12.5$ ms, which is slightly higher than the T_2 of the tetragonal phase. Our predicted T_2 is orders of magnitude larger than the experimentally-measured T_2 ($< 20 \mu\text{s}$),^{10,11} indicating that the qubit coherence is limited by a noise source other than the nuclear spin bath, such as dangling bonds that generate electric noise.

Our study elucidates the vast chemical diversity of 2D materials that can host spin qubits with long T_2 . For example, 4 out of the 15 materials with the highest T_2 contain potassium in its composition (Table 1); despite being an element with 100% spinful isotopes, the high T_2 is attributable to the relatively low g -factor (e.g. 0.26 for ^{39}K) and dilute presence in each composition. Nonetheless, it is interesting to note some common structural motifs in high- T_2 monolayers, such as square-planar units of transition metal oxides (Figures 2c-2e). A qubit's electronic structure and, therefore, properties, are influenced by the coordination symmetry of the defect center. For example, defect centers that are inversion-symmetric, such as the SiV^- center in diamond,⁴⁷ do not possess a dipole moment and are therefore less sensitive to electric field noise compared to centers that lack inversion symmetry. As a result, the choice of dopant for the spin defect center, as well as the choice of host material, can enable the design of quantum devices with a wide range of capabilities. As we discuss in detail in Section 3, the chemical richness and diversity of structural motifs embedded in these host structures can potentially enable a variety of spin defect centers with specific electronic structures and, therefore, desirable properties.

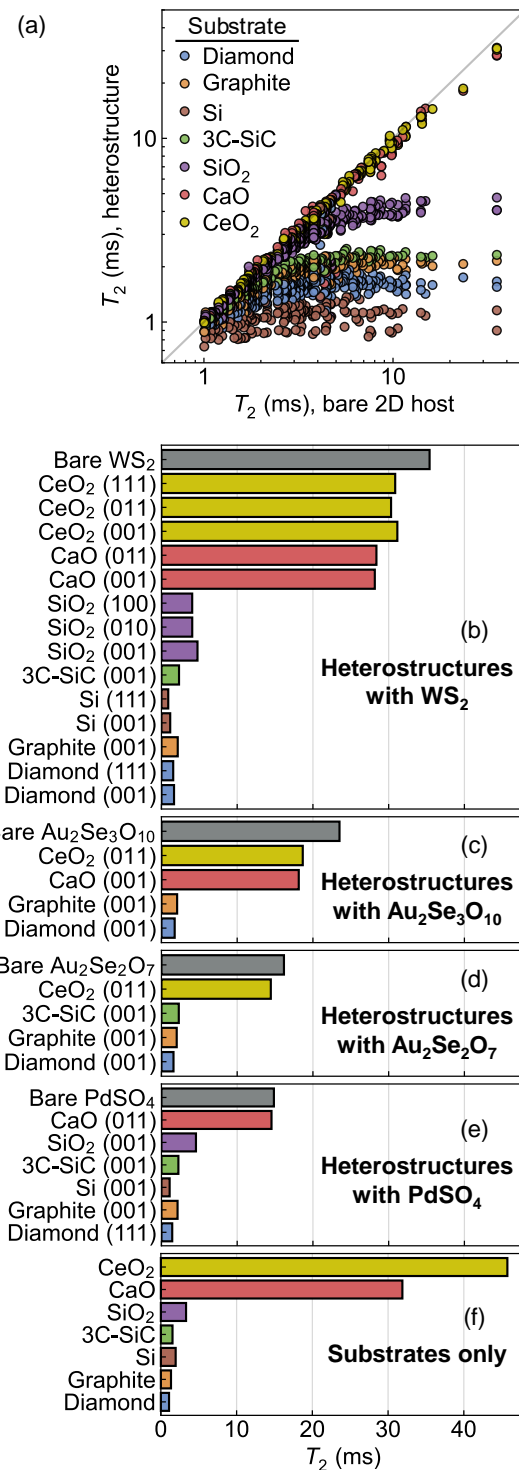


Figure 3. Coherence time of heterostructures. (a) Spin coherence time (T_2) of heterostructures compared to T_2 of the bare 2D host material. The color indicates the substrate material. (b-e) T_2 of heterostructures with WS_2 , $\text{Au}_2\text{Se}_3\text{O}_{10}$, $\text{Au}_2\text{Se}_2\text{O}_7$, and PdSO_4 . The colored bars represent heterostructures with the substrate indicated along the vertical axis, and the gray bar represents the bare 2D host. (f) T_2 of the bare substrate materials, without the 2D material.

2.3 Coherence time T_2 of heterostructures

Next, we consider heterostructures between 2D materials with $T_2 > 1$ ms and select 3D substrates cleaved along crystallographic planes. We create lattice-matched heterostructures by straining the 2D material by no more than 5%, which generates 1554 heterostructures. We use the high-throughput procedure implemented in the AiiDA-PyCCE code to compute T_2 for all heterostructures, where the qubit is placed in the 2D host material. It is important to note that we only account for decoherence driven by the nuclear spin baths of the substrate and 2D host material. While other sources of decoherence may exist, such as surface roughness and dangling bonds at the host–substrate interface,¹ the nuclear spin bath-limited T_2 can provide an upper bound estimate that reveals the role of the substrate composition on qubit coherence.

In most heterostructures, T_2 is lower than that of the bare 2D host (Figure 3a) in agreement with a previous report.³ This indicates that the nuclear spin bath of the substrate material introduces additional noise that leads to faster qubit decoherence. However, we notice that T_2 is drastically lowered by certain substrates compared to others. For example, heterostructures of WS_2 with CeO_2 and CaO appear to maintain high T_2 , almost equal to that of standalone WS_2 , whereas T_2 is nearly an order of magnitude lower than the bare 2D host when WS_2 is interfaced with other substrates, such as SiO_2 (Figure 3b). We confirm that this is not due to the strain imposed on the 2D host material, since a strain of $\pm 5\%$ varies T_2 by no more than 20% (Supplementary Note 3). Instead, not surprisingly, this can be explained by the T_2 values of the substrates themselves (Figure 3f). In particular, the T_2 of SiO_2 (3.33 ms) is nearly an order of magnitude lower than that of CeO_2 (45.7 ms) and CaO (31.9 ms), explaining the lower T_2 of heterostructures when SiO_2 is the substrate material (Figure 3b).

It is important to note that spin coherence is not always limited by the nuclear spins in the substrate material, and is instead limited by whichever component (substrate or 2D host material) is more noisy. This is clear in heterostructures of $\text{Au}_2\text{Se}_3\text{O}_{10}$, $\text{Au}_2\text{Se}_2\text{O}_7$, and PdSO_4 with CeO_2 and CaO (Figures 3c–3e). Since T_2 of the substrates (Figure 3f) are nearly double that of the 2D host materials, the primary source of decoherence, not surprisingly, is the 2D material itself. As a result, from a materials design perspective, it is critical to select a 2D host material and substrate that both have high T_2 in order to maintain high T_2 in heterostructures.

We find that when qubit decoherence is driven by hyperfine interactions with nuclear spins, different facets of the substrate material yield similar T_2 . For example, in WS_2/SiO_2 heterostructures, T_2 for the (100), (010), and (001) planes of SiO_2 are 4.06 ms, 4.07 ms, and 4.76 ms, respectively (Figure 3b). In fact, our results show that the nuclear spin bath-driven T_2 is relatively insensitive to the specific details of the heterostructural interface, whether it is confounded by the specific cleavage plane of the substrate, surface reconstruction, or even the interlayer distance between the 2D host and substrate material (more details are provided in Supplementary Note 4). These results are likely valid

only in the absence of other sources of noise that may be prevalent at the heterostructural interface, such as electric noise from dangling bonds. Hence, because additional noise sources will lead to further decoherence, heterostructures with low predicted T_2 in our study are likely unsuitable candidates for hosting qubits with robust spin coherence.

2.4 Models of coherence time T_2

Models of qubit coherence can greatly accelerate T_2 predictions. A recent work by Kanai et al.¹³ proposed a model of T_2 based on scaling laws of isotopic features, namely the g -factor, nuclear spin number, and the isotope concentration. The scaling laws, which were determined for 3D materials, indicated that the contribution from a single nuclear isotope type, i , to the coherence time can be modeled as¹³

$$T_{2,3D,i} = 1.5 \times 10^{18} |g_i|^{-1.6} I_i^{-1.1} n_i^{-1.0} (s) \quad (1)$$

where g_i is the g -factor, I_i is the nuclear spin, and n_i is the nuclear spin density. The overall T_2 of the material, assuming heteronuclear spin baths can be decoupled, is then calculated as

$$T_{2,3D}^{-\eta} = \sum_i T_{2,3D,i}^{-\eta} \quad (2)$$

where η is the stretching exponent. Importantly, the model only requires the structure of the material and basic isotopic information, which can be found in e.g. the EasySpin database.⁴⁸ The model can therefore enable rapid predictions of T_2 for large sets of materials.¹³

It is natural to ask whether the model, which was developed for 3D materials,¹³ can also predict the T_2 times of 2D materials. We initially verify that heteronuclear spin baths can be decoupled in 2D systems (Supplementary Note 5) similar to 3D systems,^{2,13,49} allowing us to test the model on 2D materials. However, using Eqs. (1) and (2) and $\eta = 2$, following the methodology of Ref. 13, we find that the T_2 predictions by the model starkly deviate from those of CCE calculations (light dots in Figure 4a), indicating that a refined model is necessary.

We find that a physically-motivated correction factor to the 3D model in Eqs. (1) and (2) can enable better predictions of T_2 for 2D hosts. This is inspired by the semi-classical model of many-body spin dynamics proposed by Davis et al.⁵⁰ where, importantly, information about the *dimensionality* of the nuclear spin environment is encoded in the coherence function. As a result, we can derive a multiplicative factor that corrects for T_2 of a qubit in a 2D spin environment, given a model of T_2 parameterized for 3D spin environments (such as the model by Kanai et al.¹³). From the derivation provided in Supplementary Note 6, we arrive at the expression

$$T_{2,2D,i} = C(\alpha_{2D}) n_i^{(2-\alpha_{2D})/3} w^{-\alpha_{2D}/3} T_{2,3D,i} \quad (3)$$

where $T_{2,2D,i}$ is the contribution from isotope i to the coherence time, and $T_{2,3D,i}$ is given by Eq. (1). The correction factor is composed of a constant $C(\alpha_{2D})$, the isotope concentration n_i (in cm^{-3}), and the thickness w of the 2D material (in cm). α_{2D} repre-

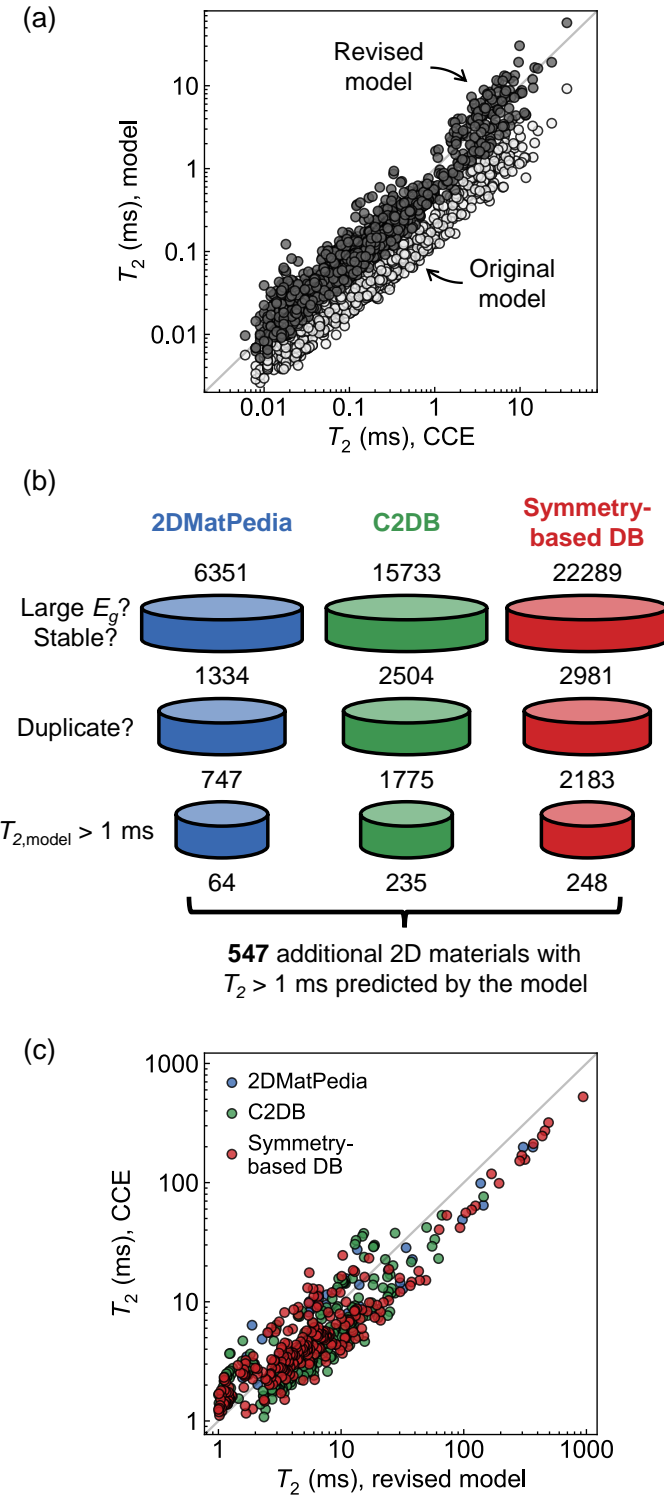


Figure 4. Model of coherence time for 2D materials. (a) Parity plot of the original (light) and revised (dark) models of the spin coherence time (T_2) for 2D materials. (b) Statistics from screening various 2D materials databases using the revised model of T_2 . (c) T_2 predicted by the revised model for monolayers across various 2D materials databases. An additional 546 monolayers with $T_1 > 1 \text{ ms}$ are found by screening these databases and verifying with CCE calculations.

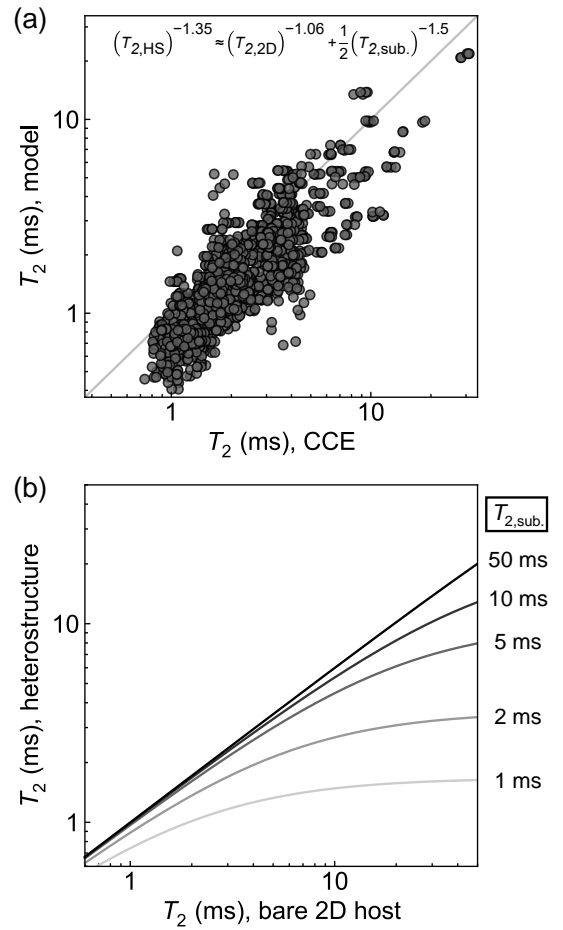


Figure 5. Model of coherence time for heterostructures. (a) The calculated coherence time (T_2) of heterostructures, compared to the T_2 predicted by the fitted model. (b) Model T_2 of heterostructures, calculated using Eq. (6), against T_2 of the bare 2D host material. Each curve corresponds to a different substrate T_2 .

sents the effective $1/r^\alpha$ interaction between the qubit and nuclear spins in 2D.⁵⁰ Although dipolar interactions in 3D are described by $\alpha_{3D} = 3$, we treat α_{2D} as a fitting parameter due to the reduced screening in 2D. The T_2 for a qubit in a 2D host ($T_{2,2D}$) can then be predicted using the formula

$$T_{2,2D}^{-3/\alpha_{2D}} = \sum_i T_{2,2D,i}^{-3/\alpha_{2D}}. \quad (4)$$

Using the data generated from our high-throughput framework, we determine that $\alpha_{2D} = 2.84$ yields the best fit to the CCE-calculated T_2 (dark dots in Figure 4a), resulting in the model

$$T_{2,2D,i} \approx 0.94 n_i^{-0.28} w^{-0.95} T_{2,3D,i} \quad (5)$$

$$T_{2,2D}^{-1.06} \approx \sum_i T_{2,2D,i}^{-1.06}$$

The fact that the fitted α_{2D} is slightly lower than the expected value from dipolar interactions in 3D ($\alpha_{3D} = 3$) is consistent with the reduced screening in a 2D nuclear spin environment.⁵¹

Using the model of T_2 in Eq. (5), we expand the search space

for 2D qubit host materials by screening various databases, in particular 2D MatPedia,¹⁷ C2DB,^{18,19} and a database constructed from symmetry considerations²⁰ (Figure 4b). We initially screen materials that are stable, have wide band gap (>0.5 eV at the level of GGA), and are non-duplicate structures (Supplementary Note 6). In total, we perform T_2 predictions on 4705 non-duplicate 2D monolayers from the three databases, from which we identify 547 host materials with $T_2 > 1$ ms (Figure 4b). We verify with CCE at order 2 that 546 of these monolayers indeed exhibit $T_2 > 1$ ms (Figure 4c), demonstrating the ability to rapidly estimate T_2 on an expansive set of 2D host materials using the model in Eq. (5). We even identify some 2D hosts with $T_2 > 100$ ms through our analysis (Figure 4c), such as monolayer FeO and CaO. Note that our simple model only requires the structure of the 2D material and basic information about the nuclear isotopes.

We can also formulate a model of T_2 for heterostructures (denoted $T_{2,HS}$) using the same semi-classical model of the coherence function proposed by Davis et al.⁵⁰ (a full derivation is given in Supplementary Note 7). We arrive at the expression

$$\left(\frac{1(s)}{T_{2,HS}(s)}\right)^{\eta_{HS}} \approx \left(\frac{1(s)}{T_{2,2D}(s)}\right)^{3/\alpha_{2D}} + \frac{1}{2} \left(\frac{1(s)}{T_{2,sub.}(s)}\right)^{3/2} \quad (6)$$

where $T_{2,2D}$ is the coherence time of the bare 2D material as given in Eq. (4), and $T_{2,sub.}$ is the coherence time of the 3D substrate, which can be calculated using Eq. (2). The “(s)” in each term represents the time unit, ensuring that the units are matched (Supplementary Note 7). η_{HS} is the stretch exponent for heterostructures and is treated as a fitting parameter. By fitting the analytical model to our data, we find that

$$\left(\frac{1(s)}{T_{2,HS}(s)}\right)^{1.35} \approx \left(\frac{1(s)}{T_{2,2D}(s)}\right)^{1.06} + \frac{1}{2} \left(\frac{1(s)}{T_{2,sub.}(s)}\right)^{1.5} \quad (7)$$

yields an appropriate fit of T_2 for heterostructures between a 2D host material and 3D substrate (Figure 5a).

The form of Eq. (6) reflects the idea that the decoherence “rate” ($\sim 1/T^\eta$) of a qubit can be expressed as a sum of all sources of decoherence, in this case the 2D host material and substrate. The model also shows that T_2 of a heterostructure can be limited by either the 2D host or substrate, depending on which component has the noisier nuclear spin environment (i.e. has lower T_2). When T_2 of the 2D host is low, T_2 of the heterostructure is limited by the spin environment of the 2D host (Figure 5b). On the other hand, when T_2 of the 2D host is high, T_2 of the heterostructure is limited by the substrate and therefore saturates with increasing $T_{2,2D}$ (Figure 5b). This result matches the findings from CCE simulations discussed earlier (Section 2.3).

3 Discussion

In this work, we develop a high-throughput computational workflow to survey the spin echo coherence times (T_2) of qubits in 2D materials and heterostructures. By applying the workflow to a set of 1173 2D materials, we identify 190 monolayers with $T_2 > 1$ ms, including WS₂, Au₂Se₃O₁₀, Au₂Se₂O₇, and PdSO₄. We then apply the workflow to 1554 lattice-matched heterostructures

between high- T_2 2D materials and substrates, where we find that placing 2D materials on low-noise substrates, such as CeO₂ and CaO, can help maintain high T_2 . In general, T_2 of a heterostructure can be limited by the nuclear spin bath of either the 2D host material or the substrate, depending on which component imposes a noisier nuclear spin environment. We then develop physically-motivated models of T_2 for 2D host materials and heterostructural systems, enabling rapid predictions based only on the structures of the 2D host and substrate materials.

To design qubit platforms with on-demand functionalities, spin defects must be identified within the host candidates. While this is beyond the scope of the present study, we can envision the possible electronic structures that can be realized through a simple symmetry analysis of structural motifs in the high- T_2 2D host candidates. For example, Au₂Se₃O₁₀, Au₂Se₂O₇, and PdSO₄ all possess transition metal complexes that are locally coordinated in a square-planar configuration (Figures 2c-e). Doping on the transition metal site, perhaps with another transition metal species with partially-filled *d*-orbitals, can potentially realize a spin-1 defect center, similar to the NV⁻ center in diamond. This is because *d*-orbital splitting in a square planar coordination leads to the formation of doublet *e_g* states, where two unpaired spins can form a spin-1 complex (Figure S8). The rich chemical variety of 2D hosts elucidated by our study, and more importantly the diversity of locally-coordinated structural motifs, can enable the design of spin qubit-based devices tailored towards particular applications.

We expect that the large amount of data from our study, and future data that can be generated using the high-throughput CCE framework or the T_2 model presented here, can enable the generative design of materials to host spin qubits with robust coherence properties. Materials design supported by artificial intelligence has become widespread and has demonstratively benefited from large-scale databases, high-throughput computation, and even simple models. Various techniques to generate hypothetical 2D materials have already been explored,⁵²⁻⁵⁴ so perhaps analogous techniques can be developed for spin qubit applications by biasing these models towards materials with high T_2 . Since the T_2 time is one of many properties in the complex, multivariate design space of spin qubit platforms, we envision that our work can be combined with other workflows to realize a comprehensive design scheme of qubit-based devices with functionalities tailored towards specific applications.

4 Methods

4.1 Cluster correlation expansion

The decoherence dynamics of a spin qubit due to magnetic noise from surrounding nuclear isotopes (i.e., the nuclear spin bath) can be described by the many-body Hamiltonian

$$\hat{H} = \gamma_e \mathbf{B} \mathbf{S} + \sum_n \mathbf{B} \gamma_n \mathbf{I}_n + \mathbf{S} \mathbf{A}_n \mathbf{I}_n + \sum_{m < n} \mathbf{I}_n \mathbf{J}_{nm} \mathbf{I}_m. \quad (8)$$

The first term represents the Zeeman splitting effect of the qubit spin \mathbf{S} due to a magnetic field \mathbf{B} . The summation is performed over all nuclear spins n with spin tensor \mathbf{I}_n . The second term represents the Zeeman splitting of the nuclear spins, the third term represents hyperfine interactions \mathbf{A}_n between the qubit spin \mathbf{S} and

nuclear spins \mathbf{I}_n , and the fourth term represents nuclear dipole-dipole interactions represented by the tensor \mathbf{J}_{nm} . Here, we do not include the effects of zero-field splitting and quadrupolar interactions, which will be considered in future studies.

The coherence function $\mathcal{L}(t)$ of a spin qubit can be computed from the Hamiltonian in Eq. (8), where

$$\mathcal{L}(t) = \left| \frac{\langle 0 | \rho(t) | 1 \rangle}{\langle 0 | \rho(0) | 1 \rangle} \right|. \quad (9)$$

Here, $\rho(t)$ is the time-dependent density matrix of the qubit spin. By applying a Hahn-echo pulse sequence, T_2 of a spin qubit can be measured and extracted by fitting $\mathcal{L}(t)$ to a stretched exponential function

$$\mathcal{L}(t) = \exp \left[- \left(\frac{t}{T_2} \right)^n \right] \quad (10)$$

where n is a stretching exponent.

The dynamics of a qubit determined by its interaction with a nuclear spin bath can be simulated using the cluster correlation expansion (CCE) approach, which considers interactions between the qubit and clusters of nuclear spins in increasing cluster size (singlets, pairs, triplets, etc.). The CCE method is widely used to model decoherence dynamics of qubits in various systems, such as the NV^- center in diamond and molecular color centers.¹⁴ Within the CCE approach, $\rho(t)$ is approximated by considering the dynamics of nuclear spin clusters with varying sizes, which allows $\mathcal{L}(t)$ to be factored into contributions from individual clusters:

$$\mathcal{L}(t) = \prod_i \widetilde{\mathcal{L}}_i(t) \prod_{ij} \widetilde{\mathcal{L}}_{ij}(t) \prod_{ijk} \widetilde{\mathcal{L}}_{ijk}(t) \dots \quad (11)$$

where $\widetilde{\mathcal{L}}_i(t)$, $\widetilde{\mathcal{L}}_{ij}(t)$, $\widetilde{\mathcal{L}}_{ijk}(t)$, etc. are the contributions from single spins i , pairs of spins ij , triplets of spins ijk , etc., respectively. It is important to note that $\mathcal{L}(t)$, and therefore T_2 , can be measured using a Hahn-echo pulse sequence in experiments, providing a direct method to compare theoretical predictions with experiments.

4.2 Computational details

We used the PyCCE software³¹ to run CCE simulations on 2D materials and heterostructures. In each system, we considered a model spin-1 defect, similar to the NV^- center in diamond. Hyperfine interactions are treated using the point-dipole approximation. A magnetic field of 5 T is applied perpendicular to the plane of the 2D material in all calculations. The g -factor is assumed to be isotropic in our calculations. Due to the statistical nature of spin dynamics, we averaged over 40 CCE simulations for each system.

There are three principal user-defined parameters within PyCCE. First, interactions between the spin qubit and nuclear bath spins are calculated only when the bath spins are within a certain cutoff radius (r_{bath}) from the qubit. Second, clusters are defined between nuclear bath spins that are within a cutoff radius (r_{dipole}) from each other. Lastly, the CCE order sets the maximum size of the clusters included in the simulation; for example, calculations of order 3 (CCE-3) considers clusters of single, pairs, and triplets of nuclear bath spins. To obtain an accurate prediction of the T_2 time, it is imperative that CCE calculations are con-

verged with respect to these three parameters. However, increasing r_{bath} , r_{dipole} , and order will also lead to longer computing time, because more nuclear bath spins are included in the calculation. This is especially a challenge when considering a large number of materials, each with their own unique set of nuclear isotopes and, therefore, different convergence criteria.

In order to strike a balance between accuracy and computing time, we employ a two-step strategy in our high-throughput workflow. First, we use a fixed, modest set of values for r_{bath} (50 Å), r_{dipole} (15 Å), and order (CCE-2) for all monolayers and predict their T_2 times. These parameters were benchmarked by Sajid and Thygesen.¹² We then rank the 2D materials based on their predicted T_2 times and perform proper convergence tests on those that exhibit $T_2 > 1$ ms. For all heterostructures, we use a fixed set of values for r_{bath} (120 Å), r_{dipole} (30 Å), and order (CCE-2) to predict T_2 .

4.3 Band gap predictions

The band gap of a 2D material is a key indicator of its ability to host deep, localized defect states. To compute these gaps from first principles, we employed density functional theory (DFT),^{55–57} which has proven highly successful at predicting ground-state properties across a wide range of materials. However, modeling the electronic structures of 2D systems remains challenging, since most exchange–correlation functionals are developed and benchmarked for bulk solids⁵⁸ and may not perform reliably for low-dimensional systems.

To overcome this limitation, we adopted the screened-exchange range-separated hybrid (SE-RSH) functional,^{29,30} which is capable of achieving good accuracy for both pristine and defective 2D materials.²⁹ Within the SE-RSH approach, the exchange energy is expressed as a linear combination of exact (Hartree–Fock) and local exchange energies,⁵⁹ with the mixing fraction determined by a spatially-dependent local dielectric function. This formulation enables the SE-RSH functional to naturally capture complex screening variations in heterogeneous systems, including 2D materials, and their influence on the electronic structure.

The SE-RSH functional has been implemented in a modified version of the Qbox code,⁶⁰ which employs a plane-wave basis set and norm-conserving pseudopotentials. We performed calculations on the relaxed 2D structures curated by the MC2D database without further structural relaxation, using supercells and Γ -point sampling, with optimized norm-conserving Vanderbilt pseudopotentials.⁶¹ The energy cutoff for the plane-wave basis set was set at 90 Ry. To minimize the interactions between neighboring supercells, a minimum of 15 Å vacuum spacing was included in our supercells.

4.4 Note on hydrated systems

In our high-throughput search of 2D materials with long T_2 times, we encountered some monolayers in which the experimentally-known 3D parent phase is naturally hydrated (i.e. have H_2O in their composition), but the hydrogen atoms are omitted from the structural CIF model likely because they could not be resolved using e.g. X-ray diffraction. This is especially preva-

lent for 3D layered systems, where there are well-defined spaces between the layers for H₂O to occupy and bind the layers. Such “dehydrated” structural models are problematic however, because they likely do not exist naturally. Moreover, because hydrogen can strongly decohere spin qubits (i.e. lower T_2) due to the high concentration of spinful nuclei, the absence of hydrogen atoms from the structure may lead to an overestimation of the T_2 time. A representative example of this is talc, which has the natural chemical formula Mg₃Si₄O₁₀(OH)₂. For the “dehydrated” structure Mg₃Si₄O₁₂ (mc2d-471), we predict $T_2 = 3.65$ ms for the monolayer; however, for the true hydrated structure (mc2d-418), we predict $T_2 = 0.085$ ms for the monolayer, which is more than an order of magnitude lower.

This requires us to check the original experimental studies of the 3D parent phases. Due to the large number of compounds considered in this study, we check by hand any 2D materials with predicted $T_2 > 1$ ms and omit those whose 3D parent phase is naturally hydrated. We do not check whether the parent phases of 2D materials with $T_2 < 1$ ms are naturally hydrated; in such cases, we expect T_2 to be lower than the predicted value for the dehydrated structure anyway.

Data and code availability

Data and scripts can be found in Zenodo at <https://doi.org/10.5281/zenodo.16997329>.

Acknowledgements

We thank Hosung Seo, Jonah Nagura, and Lien T. Le for helpful suggestions, as well as Nicola Marzari, Binbin Liu, and Kristjan Eimre for helpful discussions on the MC2D database. This work was supported by the Midwest Integrated Center for Computational Materials (MICCoM). MICCoM is part of the Computational Materials Sciences Program funded by the U.S. Department of Energy, Office of Science, Basic Energy Sciences, Materials Sciences, and Engineering Division through the Argonne National Laboratory, under contract No. DEAC02-06CH11357. This work was completed in part with resources provided by the University of Chicago’s Research Computing Center. This research used resources of the National Energy Research Scientific Computing Center (NERSC), a DOE Office of Science User Facility supported by the Office of Science of the U.S. Department of Energy under Contract No. univers using NERSC award ALCC-ERCAP0025950. This work was partly supported by JSPS Kakenhi (Grant No. 23KK0092), QST Cross-ministerial Strategic Innovation Promotion Program, JST-PRESTO (Grant No. JPMJPR21B2), and RIEC Cooperative Research Projects.

Author Contributions

M.Y.T.: methodology, software, formal analysis, investigation, data curation, writing (original draft), writing (editing). J.Z.: formal analysis, investigation, data curation, writing (editing). S.K.: writing (editing). G.G.: conceptualization, writing (editing), supervision, project administration, funding acquisition. All authors contributed to the manuscript and approved the final version.

Competing Interests

The authors declare no competing interests.

References

- 1 E. Janitz, K. Herb, L. A. Völker, W. S. Huxter, C. L. Degen and J. M. Abendroth, *J. Mater. Chem. C*, 2022, **10**, 13533.
- 2 M. Ye, H. Seo and G. Galli, *npj Comput. Mater.*, 2019, **5**, 44.
- 3 M. Onizhuk and G. Galli, *Appl. Phys. Lett.*, 2021, **118**, 154003.
- 4 B. Schuler, K. A. Cochrane, C. Kastl, E. S. Barnard, E. Wong, N. J. Borys, A. M. Schwartzberg, D. F. Ogletree, F. J. G. de Abajo and A. Weber-Bargioni, *Sci. Adv.*, 2020, **6**, eabb5988.
- 5 K. A. Cochrane, J.-H. Lee, C. Kastl, J. B. Haber, T. Zhang, A. Kozhakhmetov, J. A. Robinson, M. Terrones, J. Repp, J. B. Neaton, A. Weber-Bargioni and B. Schuler, *Nat. Commun.*, 2021, **12**, 7287.
- 6 J. C. Thomas, W. Chen, Y. Xiong, B. A. Barker, J. Zhou, W. Chen, A. Rossi, N. Kelly, Z. Yu, D. Zhou, S. Kumari, E. S. Barnard, J. A. Robinson, M. Terrones, A. Schwartzberg, D. F. Ogletree, E. Rotenberg, M. M. Noack, S. Griffin, A. Raja, D. A. Strubbe, G.-M. Rignanese, A. Weber-Bargioni and G. Hautier, *Nat. Commun.*, 2024, **15**, 3556.
- 7 H.-H. Fang, X.-J. Wang, X. Marie and H.-B. Sun, *Light Sci. Appl.*, 2024, **13**, 303.
- 8 G. Zhang, Y. Cheng, J.-P. Chou and A. Galli, *Appl. Phys. Rev.*, 2020, **7**, 031308.
- 9 A. R.-P. Montblanch, M. Barbone, I. Aharonovich, M. Atatüre and A. C. Ferrari, *Nat. Nanotechnol.*, 2023, **18**, 555.
- 10 W. Liu, S. Li, N. J. Guo, X. D. Zeng, L. K. Xie, J. Y. Liu, Y. H. Ma, Y. Q. Wu, Y. T. Wang, Z. A. Wang, J. M. Ren, C. Ao, J. S. Xu, J. S. Tang, A. Galli, C. F. Li and G. C. Guo, *Experimental observation of spin defects in van der Waals material GeS₂*, 2024, <https://arxiv.org/abs/2410.18892>.
- 11 S. Vaidya, X. Gao, S. Dikshit, Z. Fang, A. E. L. Alcca, Y. P. Chen, Q. Yan and T. Li, *Coherent Spins in van der Waals Semiconductor GeS₂ at Ambient Conditions*, 2025, <https://arxiv.org/abs/2507.05133>.
- 12 A. Sajid and K. S. Thygesen, *Phys. Rev. B*, 2022, **106**, 104108.
- 13 S. Kanai, F. J. Heremans, H. Seo, G. Wolfowicz, C. P. Anderson, S. E. Sullivan, M. Onizhuk, G. Galli, D. D. Awschalom and H. Ohno, *Proc. Natl. Acad. Sci.*, 2022, **119**, e2121808119.
- 14 M. Onizhuk and G. Galli, *Rev. Mod. Phys.*, 2025, **97**, 021001.
- 15 N. Mounet, M. Gibertini, P. Schwaller, D. Campi, A. Merkys, A. Marrazzo, T. Sohier, I. E. Castelli, A. Cepellotti, G. Pizzi and N. Marzari, *Nat. Nanotechnol.*, 2018, **13**, 246.
- 16 D. Campi, N. Mounet, M. Gibertini, G. Pizzi and N. Marzari, *ACS Nano*, 2023, **17**, 11268.

17 J. Zhou, L. Shen, M. D. Costa, K. A. Persson, S. P. Ong, P. Huck, Y. Lu, X. Ma, Y. Chen, H. Tang and Y. P. Feng, *Sci. Data*, 2019, **6**, 86.

18 S. Haastrup, M. Strange, M. Pandey, T. Deilmann, P. S. Schmidt, N. F. Hinsche, M. N. Gjerding, D. Torelli, P. M. Larsen, A. C. Riis-Jensen, J. Gath, K. W. Jacobsen, J. Jørgen Mortensen, T. Olsen and K. S. Thygesen, *2D Mater.*, 2018, **5**, 042002.

19 M. N. Gjerding, A. Taghizadeh, A. Rasmussen, S. Ali, F. Bertoldo, T. Deilmann, N. R. Knøsgaard, M. Kruse, A. H. Larsen, S. Manti, T. G. Pedersen, U. Petralanda, T. Skovhus, M. K. Svendsen, J. J. Mortensen, T. Olsen and K. S. Thygesen, *2D Mater.*, 2021, **8**, 044002.

20 H.-C. Wang, J. Schmidt, M. A. L. Marques, L. Wirtz and A. H. Romero, *2D Mater.*, 2023, **10**, 035007.

21 Campi, Davide, Mounet, Nicolas, Gibertini, Marco, Pizzi, Giovanni and Marzari, Nicola, *The Materials Cloud 2D database (MC2D)*, 2022, <https://archive.materialscloud.org/record/2022.84>.

22 A. Belsky, M. Hellenbrandt, V. L. Karen and P. Luksch, *Acta Crystallogr. B*, 2002, **58**, 364.

23 D. Zagorac, H. Müller, S. Ruehl, J. Zagorac and S. Rehme, *J. Appl. Crystallogr.*, 2019, **52**, 918.

24 S. Gražulis, D. Chateigner, R. T. Downs, A. F. T. Yokochi, M. Quirós, L. Lutterotti, E. Manakova, J. Butkus, P. Moeck and A. Le Bail, *J. Appl. Crystallogr.*, 2009, **42**, 726.

25 S. Gražulis, A. Daškevič, A. Merkys, D. Chateigner, L. Lutterotti, M. Quirós, N. R. Serebryanaya, P. Moeck, R. T. Downs and A. Le Bail, *Nucleic Acids Res.*, 2012, **40**, D420.

26 P. Villars, N. Onodera and S. Iwata, *J. Alloy Compd.*, 1998, **279**, 1.

27 T. Alkathiri, K. Xu, B. Y. Zhang, M. W. Khan, A. Jannat, N. Syed, A. F. M. Almutairi, N. Ha, M. M. Y. A. Alsaif, N. Pillai, Z. Li, T. Daeneke and J. Z. Ou, *Small Sci.*, 2022, **2**, 2100097.

28 J. R. Weber, W. F. Koehl, J. B. Varley, A. Janotti, B. B. Buckley, C. G. Van de Walle and D. D. Awschalom, *Proc. Natl. Acad. Sci.*, 2010, **107**, 8513.

29 J. Zhan, M. Govoni and G. Galli, *J. Chem. Theory Comput.*, 2023, **19**, 5851.

30 J. Zhan, M. Govoni and G. Galli, *Phys. Rev. Mater.*, 2025, **9**, 053808.

31 M. Onizhuk and G. Galli, *Adv. Theory Simul.*, 2021, **4**, 2100254.

32 S. P. Huber, S. Zoupanos, M. Uhrin, L. Talirz, L. Kahle, R. Häuselmann, D. Gresch, T. Müller, A. V. Yakutovich, C. W. Andersen, F. F. Ramirez, C. S. Adorf, F. Gargiulo, S. Kumbhar, E. Passaro, C. Johnston, A. Merkys, A. Cepellotti, N. Mounet, N. Marzari, B. Kozinsky and G. Pizzi, *Sci. Data*, 2020, **7**, 300.

33 M. Uhrin, S. P. Huber, J. Yu, N. Marzari and G. Pizzi, *Comp. Mater. Sci.*, 2021, **187**, 110086.

34 <https://github.com/mathtoriyama/aiida-pycce>.

35 S. Alvarez, *Dalton Trans.*, 2013, **42**, 8617.

36 A. Zur and T. C. McGill, *J. Appl. Phys.*, 1984, **55**, 378.

37 K. Mathew, A. K. Singh, J. J. Gabriel, K. Choudhary, S. B. Sinnott, A. V. Davydov, F. Tavazza and R. G. Hennig, *Comp. Mater. Sci.*, 2016, **122**, 183.

38 M. I. Bakti Utama, Q. Zhang, J. Zhang, Y. Yuan, F. J. Belarre, J. Arbiol and Q. Xiong, *Nanoscale*, 2013, **5**, 3570.

39 H. Shi, H. Pan, Y.-W. Zhang and B. I. Yakobson, *Phys. Rev. B*, 2013, **87**, 155304.

40 W. Chen, S. M. Griffin, G.-M. Rignanese and G. Hautier, *Phys. Rev. B*, 2022, **106**, L161107.

41 A. Chernikov, T. C. Berkelbach, H. M. Hill, A. Rigosi, Y. Li, B. Aslan, D. R. Reichman, M. S. Hybertsen and T. F. Heinz, *Phys. Rev. Lett.*, 2014, **113**, 076802.

42 B. Zhu, X. Chen and X. Cui, *Sci. Rep.*, 2015, **5**, 9218.

43 A. Avsar, C.-Y. Cheon, M. Pizzochero, M. Tripathi, A. Ciarrocchi, O. V. Yazyev and A. Kis, *Nat. Commun.*, 2020, **11**, 4806.

44 M. A. Aslam, S. Leitner, S. Tyagi, A. Proviñas, V. Tkachuk, E. Pavlica, M. Dienstleider, D. Knez, K. Watanabe, T. Taniguchi, D. Yan, Y. Shi, T. Knobloch, M. Waltl, U. Schwingenschlögl, T. Grasser and A. Matković, *Nano Lett.*, 2024, **24**, 6529.

45 Y. S. Cho, D. Rhee, J. Lee, S. Y. Jung, J. Eom, V. Mazanek, B. Wu, T. Kang, S. Baek, H. Choi, Z. Sofer, S. Lee and J. Kang, *EcoMat*, 2023, **5**, e12358.

46 T. Dahmen, P. Rittner, S. Böger-Seidl and R. Gruehn, *J. Alloy Compd.*, 1994, **216**, 11.

47 A. Sipahigil, K. Jahnke, L. Rogers, T. Teraji, J. Isoya, A. Zibrov, F. Jelezko and M. Lukin, *Phys. Rev. Lett.*, 2014, **113**, 113602.

48 S. Stoll and A. Schweiger, *J. Magn. Reson.*, 2006, **178**, 42.

49 H. Seo, A. L. Falk, P. V. Klimov, K. C. Miao, G. Galli and D. D. Awschalom, *Nat. Commun.*, 2016, **7**, 12935.

50 E. J. Davis, B. Ye, F. Machado, S. A. Meynell, W. Wu, T. Mittiga, W. Schenken, M. Joos, B. Kobrin, Y. Lyu, Z. Wang, D. Bluvstein, S. Choi, C. Zu, A. C. B. Jayich and N. Y. Yao, *Nat. Phys.*, 2023, **19**, 836.

51 R. Y. Kezerashvili and V. Y. Kezerashvili, *Phys. Rev. B*, 2022, **105**, 205416.

52 Y. Song, E. M. D. Siriwardane, Y. Zhao and J. Hu, *ACS Appl. Mater. Inter.*, 2021, **13**, 53303.

53 P. Lyngby and K. S. Thygesen, *npj Comput. Mater.*, 2022, **8**, 232.

54 R. Dong, Y. Song, E. M. D. Siriwardane and J. Hu, *Adv. Intel. Syst.*, 2023, **5**, 2300141.

55 P. Hohenberg and W. Kohn, *Phys. Rev.*, 1964, **136**, B864.

56 W. Kohn and L. J. Sham, *Phys. Rev.*, 1965, **140**, A1133.

57 A. M. Teale, T. Helgaker, A. Savin, C. Adamo, B. Aradi, A. V. Arbuznikov, P. W. Ayers, E. J. Baerends, V. Barone, P. Calaminici, E. Cancès, E. A. Carter, P. K. Chattaraj, H. Chermette, I. Ciofini, T. D. Crawford, F. De Proft, J. F. Dobson, C. Draxl, T. Frauenheim, E. Fromager, P. Fuentealba, L. Gagliardi, G. Galli, J. Gao, P. Geerlings, N. Gidopoulos, P. M. W. Gill, P. Gori-Giorgi, A. Görling, T. Gould, S. Grimme, O. Gritsenko, H. J. A. Jensen, E. R. Johnson, R. O. Jones, M. Kaupp, A. M. Köster, L. Kronik, A. I. Krylov, S. Kvaal, A. Laestadius, M. Levy, M. Lewin, S. Liu, P.-F. Loos, N. T. Maitra, F. Neese, J. P. Perdew, K. Pernal, P. Pernot, P. Piecuch, E. Rebolini, L. Reining, P. Romaniello, A. Ruzsinszky, D. R. Salahub, M. Scheffler, P. Schwerdtfeger, V. N. Staroverov, J. Sun, E. Tellgren, D. J. Tozer, S. B. Trickey, C. A. Ullrich, A. Vela, G. Vignale, T. A. Wesolowski, X. Xu and W. Yang, *Phys. Chem. Chem. Phys.*, 2022, **24**, 28700.

58 F. Tran and P. Blaha, *Phys. Rev. Lett.*, 2009, **102**, 226401.

59 S. Ghosh, P. Verma, C. J. Cramer, L. Gagliardi and D. G. Truhlar, *Chem. Rev.*, 2018, **118**, 7249.

60 F. Gygi, *IBM Journal of Research and Development*, 2008, **52**, 137.

61 D. R. Hamann, *Phys. Rev. B*, 2013, **88**, 085117.